

## Two-dimensional bispectral analysis of drift wave turbulence in a cylindrical plasma

T. Yamada,<sup>1,a)</sup> S.-I. Itoh,<sup>2</sup> S. Inagaki,<sup>2</sup> Y. Nagashima,<sup>1</sup> S. Shinohara,<sup>3</sup> N. Kasuya,<sup>4</sup> K. Terasaka,<sup>3</sup> K. Kamataki,<sup>3</sup> H. Arakawa,<sup>3</sup> M. Yagi,<sup>2</sup> A. Fujisawa,<sup>2</sup> and K. Itoh<sup>4</sup>

<sup>1</sup>Graduate School of Frontier Sciences, The University of Tokyo, Kashiwa 277-8561, Japan

<sup>2</sup>Research Institute for Applied Mechanics, Kyushu University, Kasuga 816-8580, Japan

<sup>3</sup>Interdisciplinary Graduate School of Engineering Sciences, Kyushu University, Kasuga 816-8580, Japan

<sup>4</sup>National Institute for Fusion Science, Toki 509-5292, Japan

(Received 12 May 2009; accepted 10 March 2010; published online 27 May 2010)

Bispectral analysis and multichannel measurement are becoming attractive investigation tools in plasma fluctuation studies. In the Large Mirror Device-Upgrade, the measurement of fluctuations in the ion saturation-current with a 64-channel poloidal Langmuir probe array was performed. The two-dimensional (2D) (poloidal wave number and frequency) power spectrum showed a number of pronounced peaks and broadband fluctuations in the poloidal wave number-frequency space. We applied 2D bispectral analysis, which considers both the matching conditions of poloidal wave number and frequency, to the spatiotemporal waveform, and confirmed the nonlinear couplings between coherent-coherent, coherent-broadband, and broadband-broadband fluctuation components. More than ten peaks were revealed to have as their origins only three original parent modes generated in the plasma. Comparison between the theoretical estimate and experimental observation for the bicoherence showed good agreement. © 2010 American Institute of Physics.

[doi:[10.1063/1.3429674](https://doi.org/10.1063/1.3429674)]

### I. INTRODUCTION

Anomalous transport in magnetized plasmas is a significant obstacle to achieving thermonuclear fusion. Drift wave turbulence is an important feature of anomalous transport that requires further investigation. Nonlinear interactions between drift waves are believed to determine the saturation or steady state of turbulence. Recently, theories<sup>1</sup> and simulations<sup>2-4</sup> have predicted that the nonlinear couplings between drift waves should generate mesoscale structures, such as zonal flows and streamers, which have a strong impact on the anomalous transport. Experimental confirmation of the fundamental nonlinear processes and dynamics in a drift wave system is needed to give a concrete basis to these predictions.

Easily accessible plasma devices are necessary to investigate the fundamental processes occurring in drift wave turbulence. Experiments have been carried out in a number of linear cylindrical devices such as CLM,<sup>5,6</sup> CSDX,<sup>7-9</sup> Hanbit,<sup>10</sup> HYPER-I,<sup>11</sup> KIWI,<sup>12,13</sup> MIRABELLE,<sup>14</sup> Q<sub>T</sub>-Upgrade machine,<sup>15</sup> VINETA,<sup>16,17</sup> and toroidal devices such as CHS,<sup>18</sup> H1-Heliac,<sup>19,20</sup> JFT-2M,<sup>21</sup> TJ-II,<sup>22</sup> TJ-K,<sup>23-26</sup> and TORPEX.<sup>27</sup> In these low temperature devices, several multipoint Langmuir probe systems have been developed to measure wave numbers. Examples include the 64-channel poloidal probe array<sup>12-14,16,17,23,24</sup> and 8×8 channel two-dimensional (2D) array in TJ-K.<sup>25,26</sup> A number of fundamental processes associated with drift waves and their turbulence have been elucidated using these innovative Langmuir probe systems, e.g., the formation processes of drift wave turbulence,<sup>13</sup> mode-selective control of drift wave

turbulence,<sup>14</sup> drift wave excitation by ion flow velocity shear,<sup>15</sup> the nature of three-dimensional drift waves,<sup>16</sup> the transition from drift to interchange instabilities,<sup>27</sup> and sheared flow generation by drift wave turbulence via Reynolds stress.<sup>6-8,18,22</sup>

A number of numerical analysis techniques have been developed to quantitatively clarify the nonlinear interactions occurring in turbulence. One such method, bispectral analysis,<sup>28</sup> can quantify the strength of the nonlinear coupling between three waves that satisfy the frequency and wave number matching conditions. Studies on drift wave turbulence using bispectral analysis have shown many interesting results.<sup>5,10,21</sup> Recent development of multichannel diagnostics has extended the domain for bispectral analysis from frequency-only to simultaneous frequency and wave number measurements.<sup>17,25</sup> By assuming three-wave coupling, such as that described by the Hasegawa-Mima equation, the energy transfer direction between the waves can only be determined via bispectral analysis.<sup>29,30</sup> Using this method, energy transfer directions were evaluated in the frequency domain<sup>9</sup> and also in wave number domains.<sup>25</sup> Another method that is free of assumptions based on a particular model of three-wave couplings or quadratic nonlinearity is the amplitude correlation technique (ACT). This technique has been proposed to determine the direction of energy transfer.<sup>19,20,31</sup>

The Large Mirror Device-Upgrade (LMD-U) is a linear cylindrical device at Kyushu University, which has been constructed for investigation on drift wave turbulence.<sup>32</sup> A 64-channel poloidal Langmuir probe array<sup>33</sup> has been installed to take 2D measurements in poloidal wave number and frequency, in order to clarify the structure of nonlinear coupling in drift wave turbulence. The measurements have provided several interesting results,<sup>34-36</sup> such as the first experimental

<sup>a)</sup>Electronic mail: [takuma@k.u-tokyo.ac.jp](mailto:takuma@k.u-tokyo.ac.jp).

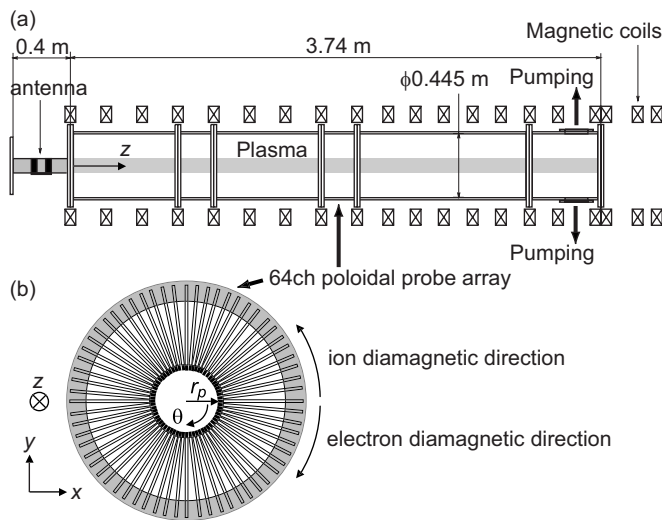


FIG. 1. Schematic view of (a) the LMD-U linear plasma device and (b) 64-channel poloidal probe array. Axial magnetic field is generated in the positive  $z$  direction. All the probe tips are precisely aligned on a single metal plate.

identification of streamers. In this paper, we present a full description of the results from the 2D bispectral analysis, e.g., the existence of nonlinear coupling between peaks and broadband fluctuations. We also determine the energy transfer direction by applying ACT, demonstrating the power of diagnostics with wave number decomposition to resolve the fine structure of nonlinear interactions. New results presented in this paper are the following: first, a clear demonstration of the presence of nonlinear couplings between quasiscoherent mode and broadband fluctuations; second, the discovery of a region where the nonlinear couplings between broadband fluctuations are remarkable; and third, a comparison between theoretical estimates and experimental observations of bicoherence. The use of bicoherence analysis on poloidally decomposed fluctuations provides a more quantitative understanding of nonlinear interaction between drift wave fluctuations.

## II. LARGE MIRROR DEVICE-UPGRADE

The LMD-U (Ref. 32) vacuum vessel has an axial length of 3.74 m, as shown in Fig. 1. The radial direction,  $r$ , is from the plasma center toward the outside, the poloidal direction,  $\theta$ , is clockwise when viewed from the plasma source to the opposite end, and the axial direction,  $z$ , is from the source to the end. A straight magnetic field (0.01–0.15 T) is generated in the positive axial direction. Therefore, the positive poloidal direction is the electron diamagnetic direction. The LMD-U plasma is generated by radio-frequency waves (7 MHz/3 kW) inside a quartz tube with an inner diameter of 95 mm, thus, the plasma radius is about 50 mm. The quartz tube is filled with argon gas with a pressure of 0.2–0.8 Pa. For typical discharge conditions (magnetic field of 0.09 T and argon pressure of 0.27 Pa), the peak electron density of the plasma is  $8 \times 10^{18} \text{ m}^{-3}$ . The electron temperature is about 3 eV, and is nearly uniform inside the plasma ( $3 \pm 0.5$  eV). Figure 2 shows typical 2D and radial profiles

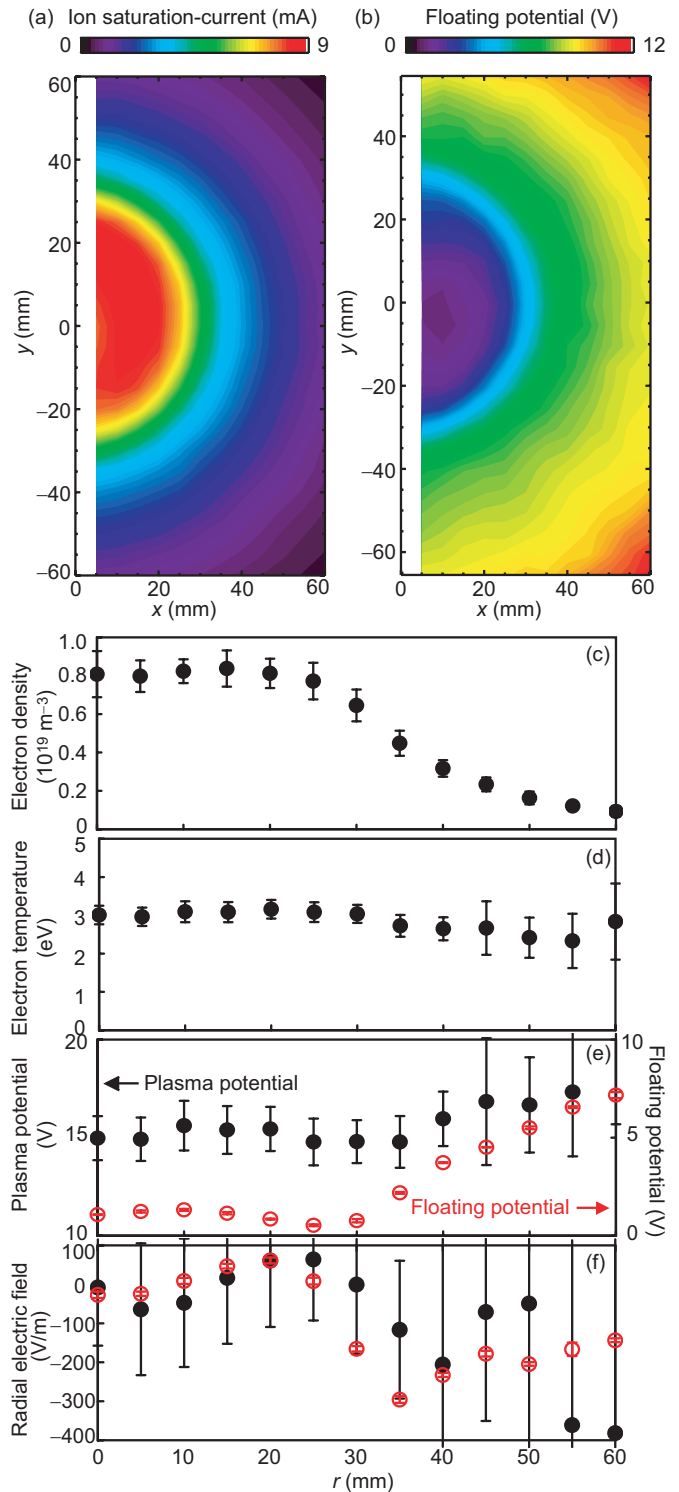


FIG. 2. (Color) 2D and radial profiles of a typical LMD-U plasma. 2D profiles of (a) ion saturation-current and (b) floating potential are shown in the domain of  $5 \text{ mm} \leq x \leq 60 \text{ mm}$  and  $|y| \leq \sim 60 \text{ mm}$ .  $x$  and  $y$  directions are introduced in Fig. 1(b). Radial profiles are given for (c) electron density, (d) electron temperature, (e) plasma (closed, black)/floating (open, red) potentials, and (f) radial electric field calculated from the plasma (closed, black)/floating (open, red) potentials. The discharge condition (magnetic field, argon pressure) is (0.09 T and 0.27 Pa).

of the ion saturation-current, floating potential, electron density, electron temperature, plasma potential, and radial electric field measured with a 2D mobile probe. Note that the profiles in Fig. 2 are taken under conditions identical to the

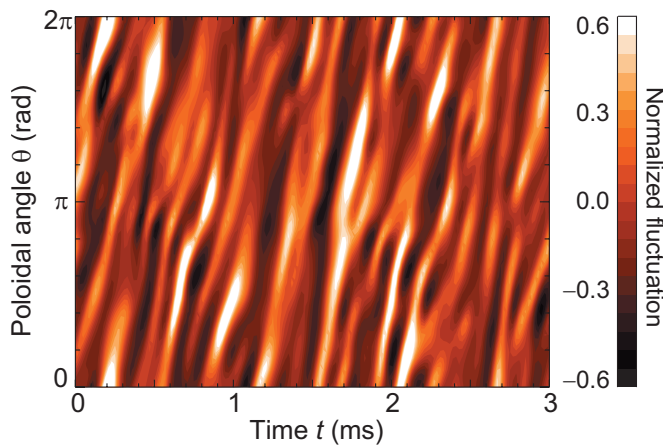


FIG. 3. (Color) Spatiotemporal behavior of normalized ion saturation-current fluctuation,  $\tilde{I}_{is}/\bar{I}_{is}$ , measured with the 64-channel poloidal probe array. The discharge condition (magnetic field and argon pressure) is (0.09 T and 0.27 Pa).

plasmas analyzed in Secs. III–V, but with better spatial resolution. The electron density gradient is steepest around  $r=30$  mm.

A 64-channel poloidal Langmuir probe array<sup>33</sup> is installed on LMD-U at  $r_p=40$  mm and  $z=1885$  mm. Figure 1(b) is a schematic view of the 64-channel poloidal probe array. All of the probe tips are mounted on a single annular metal plate with the probe tips aligned precisely enough to apply 2D spectral and bispectral analyses. Moreover, the metal plate and probe tips can be moved as a single unit in the  $r$ - $\theta$  plane, so that the probe center can be aligned to the plasma center. The alignment is important to avoid the generation of spurious modes in the 2D spectral analysis results.<sup>33</sup> Ion saturation-current and floating potential can be measured with this probe array. In this paper, we measured the fluctuation of the ion saturation-current, which is related to the fluctuation of the electron density when the electron temperature is constant.

The resistive drift wave mode is excited in the LMD-U plasma by the density gradient. The formation processes of drift wave turbulence were studied on KIWI.<sup>7</sup> In the case of LMD-U, the excited mode changes into drift wave turbulence when the magnetic field is raised above 0.04 T or the argon pressure is reduced to less than 0.4 Pa.<sup>35</sup> The spatiotemporal pattern of the fluctuation is measurable with the 64-channel poloidal probe array. The waveform of nonturbulent plasma without turbulence is a periodical pattern. For instance, when the discharge conditions (magnetic field and argon pressure) are (0.02 T and 0.27 Pa), the waveform shows an almost sinusoidal wave propagation in the electron diamagnetic direction with the poloidal mode number  $m=3$ . In contrast, turbulent plasma has a complex waveform which is aperiodic. Figure 3 shows an example of the spatiotemporal waveform of the normalized ion saturation-current fluctuation,  $\tilde{I}_{is}/\bar{I}_{is}$ , in a turbulent plasma with the discharge conditions are (0.09 T and 0.27 Pa). The waveform consists of many frequency components. We deduce that the dominant fluctuation component in turbulence such as that shown in Fig. 3 originates from resistive drift waves for the following

reason. As is reported in Ref. 35, the radial power spectrum profile of the normalized ion saturation-current fluctuation was measured using a radially mobile probe. The fluctuations above 2 kHz have a maximum amplitude around  $r=30$  mm, where the density gradient is steep. In addition, the peak frequencies of the fluctuations continuously change as the magnetic field increases from 0.03 to 0.09 T, while the sinusoidal oscillation at  $B=0.03$  T was identified as a resistive drift wave instability.<sup>32</sup> (More precisely, in the case of the sinusoidal oscillation at  $B=0.03$  T, the density fluctuation leads the potential fluctuation by  $10^\circ$ – $30^\circ$ , the normalized density and potential fluctuation levels are approximately the same, and the observed frequency is close to the linear frequency.<sup>32</sup>) Thus, the fluctuation of the peak frequency is considered to be the evolution of resistive drift instabilities. These observations support the hypothesis that the fluctuations over 2 kHz originate from resistive drift waves, that they are the drift wave turbulence. Fluctuation components of the frequency less than 2 kHz do not have a peak around  $r=30$  mm and are believed to be unrelated to linear drift waves.<sup>35</sup>

### III. SPECTRAL ANALYSIS IN LMD-U

The 2D waveform,  $z(\theta, t)$ , of the normalized ion saturation-current fluctuation was measured with the 64-channel poloidal probe array with a time resolution of  $\Delta t=1$   $\mu$ s. A 2D Fourier transformation was applied to  $z(\theta, t)$  to calculate the 2D power spectrum,  $S(m, f)$ , where  $m$  is the poloidal mode number and  $f$  is the frequency (see Appendix A for the calculation method). The temporal window of the Fourier transformation was 10 ms so that the frequency resolution was  $\Delta f=100$  Hz. When the discharge conditions were (0.02 T and 0.27 Pa), the 2D power spectrum,  $S(m, f)$ , the drift wave mode had a single peak at  $(m, f)=(3, 4.2$  kHz). Note that the poloidal mode number,  $m$ , is set to be  $m \geq 0$ , and positive frequency means that the propagation occurs in the electron diamagnetic direction. Therefore,  $(m, f)=(3, 4.2$  kHz) indicates that the propagation occurs in the electron diamagnetic direction in the laboratory frame.

As shown in Fig. 3, the waveform,  $z(\theta, t)$ , shows drift wave turbulence when the magnetic field is increased to 0.09 T. Figure 4(a) shows a contour of the 2D power spectrum  $S(m, f)$  for this case. It is an ensemble-average of 300 time windows to refine the statistics. A number of modes can be seen on the broadband fluctuations in the 2D power spectrum. The coordinates of the modes,  $(m, f)$ , are (A: 1, 2.8 kHz), (B: 2, 3.2 kHz), (C: 1,  $-0.9$  kHz), (D: 2, 5.6 kHz), (E: 2, 1.9 kHz), (F: 1, 4.1 kHz), (G: 3, 8.4 kHz), (H: 3, 4.7 kHz), (I: 2, 6.9 kHz), and (J: 3, 9.7 kHz). Though they are not visible in Fig. 4(a), the modes (K: 2,  $-1.8$  kHz), (L: 1, 0.4 kHz), (M: 1, 6.5 kHz), (N: 2, 9.3 kHz), and (O: 3, 1.0 kHz) are identifiable in Fig. 4(b), which shows the same spectrum with a logarithmic vertical scale. In Sec. IV, the modes almost buried in the broadband spectrum will become obvious by carrying out the bicoherence analysis.

The appearance of more than ten peaks in the  $m$ - $f$  plane may appear to be a complicated phenomenon. However, we have found that many of the peaks originate from the cou-

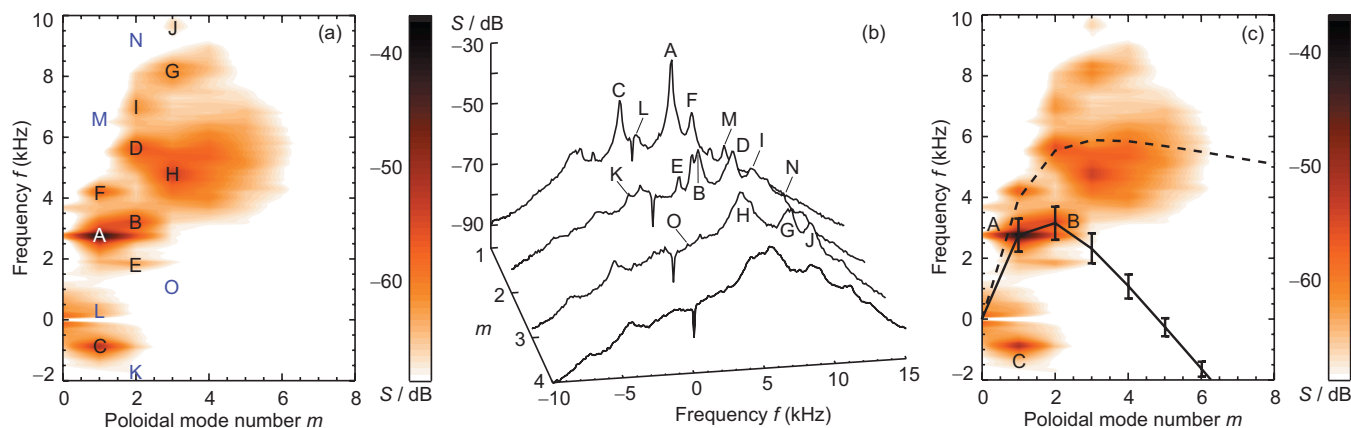


FIG. 4. (Color) (a) Contour plot ( $\text{Hz}^{-1}$ ) of 2D power spectrum of normalized ion saturation-current fluctuation in LMD-U. The discharge condition (magnetic field and argon pressure) is (0.09 T and 0.27 Pa). Positive  $f$  indicates propagation in the electron diamagnetic direction. The frequency resolution is 100 Hz. A number of peaks that together satisfy the matching conditions are observed. (b) The same data as (a), but plotted with a logarithmic vertical scale. (c) The same graph as (a). Dashed and solid lines are the linear dispersion relation calculated by numerical simulation. The dashed line assumes no dc radial electric field, and the solid line assumes a specified dc radial electric field, the value of which is set by adjusting mode (a) to the  $m=1$  eigenfrequency.

plings between a small number of parent modes. The original parent modes must be driven by linear instabilities such as the drift mode, while quasimodes or child modes are not driven by linear instabilities, but can be excited by two other modes via nonlinear couplings.<sup>37</sup> We call the child modes quasimodes, since they are not linear instability modes. The peaks satisfying the matching condition in the wave number and frequency are as follows: (D=A+A), (E=A+C), (B=C+F), (G=A+D), (H=C+D), (H=A+E), (I=A+F), (J=A+I), (K=C+C), (B=A+L), (D=C+M), (N=A+M), and (O=C+E). The modes (D) and (G) are the higher harmonics of the mode (A), while the mode (K) is the higher harmonic of the mode (C). These higher harmonics are also quasimodes generated by self-nonlinear couplings. The broadband fluctuations are also assumed to be generated by multiple nonlinear couplings between the modes and the broadband fluctuations themselves. The bandwidth of a quasimode is broader than its parent modes after the nonlinear coupling process. Analysis of nonlinear coupling is described later in this paper.

The above matching conditions allow various expressions. For example, (E=A+C) can be rewritten as (A=E+C\*), (C=A\*+E), and so on, where the mode with the opposite mode number and frequency is indicated by an asterisk. Satisfying the matching condition does not guarantee the existence of a nonlinear coupling between the modes, but is a necessary condition. The existence of the nonlinear mode couplings are confirmed using bicoherence analysis in Sec. IV. Moreover, a careful investigation of the above-mentioned combinations of modes suggests that only three irreducible modes (or three parent modes) are needed to excite all the observed modes through nonlinear couplings. Two combinations of the three original parent modes are plausible, (A, B, and C) and (A, C, and F), since these four modes are relatively coherent and strong.

The linear dispersion of the drift waves can be predicted with a numerical simulation code<sup>4</sup> to determine the parent modes. The lines in Fig. 4(c) show the dispersion relations superimposed on the 2D power spectrum,  $S(m, f)$ , which is

the same as in Fig. 4(a). The dashed line shows the case with no poloidal rotation (the eigenfrequency at the plasma rotating frame), while the solid line shows the case with a poloidal velocity of 300 m/s in the ion diamagnetic direction, which gives a Doppler shifted frequency of  $k_{\theta}v_{\theta}/2\pi = -1.2$  kHz at the  $m=1$  mode. The error bars on the solid line are the standard deviations of several results using possible electron density profiles determined from the radially mobile probe measurement. With this rotation assumed, mode (A) is located exactly on the dispersion relation in the laboratory frame. Moreover, it is found that mode (B) also happens to be on the dispersion relation. If this rotation is dominated by the  $E \times B$ -drift, the corresponding electric field is 27 V/m. Note that from Fig. 2(f), the measured radial electric field is approximately -200 V/m, however, an experiment in a linear cylindrical device has reported that a clear difference between the  $E \times B$  drift and real rotation velocity due to the ion force caused by charge exchange with the background neutrals.<sup>11</sup>

Finally, in order to show the accuracy of 2D spectral analysis using multichannel probes, one-dimensional (1D) power spectra  $S(f)$  and  $S(m)$  are calculated, as shown in Fig. 5, by integrating the 2D power spectrum  $S(m, f)$  in terms of mode number,  $m$ , or frequency,  $f$ . We have confirmed that the 1D power spectrum  $S(f)$  is essentially the same as the result from a single probe measurement. Many peaks which can be seen in  $S(m, f)$  become obscure in the 1D spectra,  $S(f)$  and  $S(m)$ . This fact clearly demonstrates an advantage of multichannel probe systems. In other words, the modes that are not discernible in 1D power spectrum are unambiguously resolved by decomposing the 1D spectrum into mode number and frequency. Finally, it should be mentioned that both  $S(f)$  and  $S(m)$  have the same decay laws,  $S(f) \propto f^{-7.0}$  and  $S(m) \propto m^{-7.0}$ . For reference, it has been reported that the decay indices of the power in CSDX (Ref. 7) and KIWI (Ref. 12) are  $S \propto k^{-5.4}$  and  $k^{-7.2}$ , respectively. The characteristics of the power spectrum in LMD-U should be close to that of KIWI.

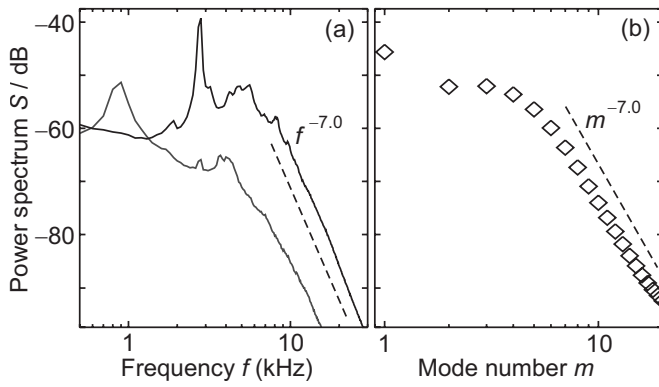


FIG. 5. 1D power spectra (a)  $S(f)$  and (b)  $S(m)$ , which are calculated by integrating  $S(m, f)$ . Black and gray lines in (a) indicate spectra with positive and negative frequencies, respectively.

#### IV. BISPECTRAL ANALYSIS IN LMD-U

The next task is to confirm the existence of nonlinear couplings postulated in Sec. III by using 2D bispectral analysis. 1D bispectral analysis in frequency space has been performed in many cases.<sup>5,10,21</sup> The 2D bispectral analysis should be more effective since it can evaluate the coupling strength between three genuine modes by removing the mode degeneracy at a frequency in mode number space. However, there are few cases of multidimensional bispectral

analyses<sup>17,25</sup> owing to the difficulty of acquiring precise multipoint measurements of the wave number.

The 2D Fourier spectrum,  $Z(m, f)$ , of the normalized ion saturation-current fluctuation was calculated for the three genuine modes satisfying the matching condition both in poloidal mode number and frequency;  $(m_1, f_1)$ ,  $(m_2, f_2)$ , and  $(m_3, f_3)$  with  $m_1 + m_2 = m_3$ ,  $f_1 + f_2 = f_3$  (see Appendix A for the calculation method). Figure 6 shows three examples of the bicoherence analyses applied to  $Z(m, f)$ . In Fig. 6(a), both  $m_1$  and  $m_2$  are fixed to 1 (therefore,  $m_3 = 2$ ). The horizontal and vertical axes are  $f_1$  and  $f_2$ , respectively, which are in the range of  $-20 \text{ kHz} \leq f_{1,2} \leq 20 \text{ kHz}$  (therefore,  $-40 \text{ kHz} \leq f_3 \leq 40 \text{ kHz}$ ). The squared bicoherence,  $b^2$ , with the mode number matching condition of  $(m_1, m_2, m_3) = (1, 1, 2)$  is plotted for an ensemble of 300 time windows (each time window is 10 ms long), so that the confidence level is  $0.003 (= 1/300)$ . Figure 6(b) is a magnified plot of Fig. 6(a) showing the range of  $-10 \text{ kHz} \leq f_{1,2} \leq 10 \text{ kHz}$ . The self-nonlinear coupling (D=A+A) shown by the circle labeled 1 at  $f_1 = f_2 = 2.8 \text{ kHz}$ , is confirmed because the bicoherence value ( $b^2 = 0.04$ ) is above the confidence level. The other circles with numbers in the figure show the existence of the nonlinear mode couplings expected in Sec. III. The confirmed nonlinear couplings are (2: E=A+C), (3: B=C+F), (4: I=A+F), (5: K=C+C), (6: B=A+L), (7: D=C+M), and (8: N=A+M). Figures 6(c) and 6(d) show the squared bico-

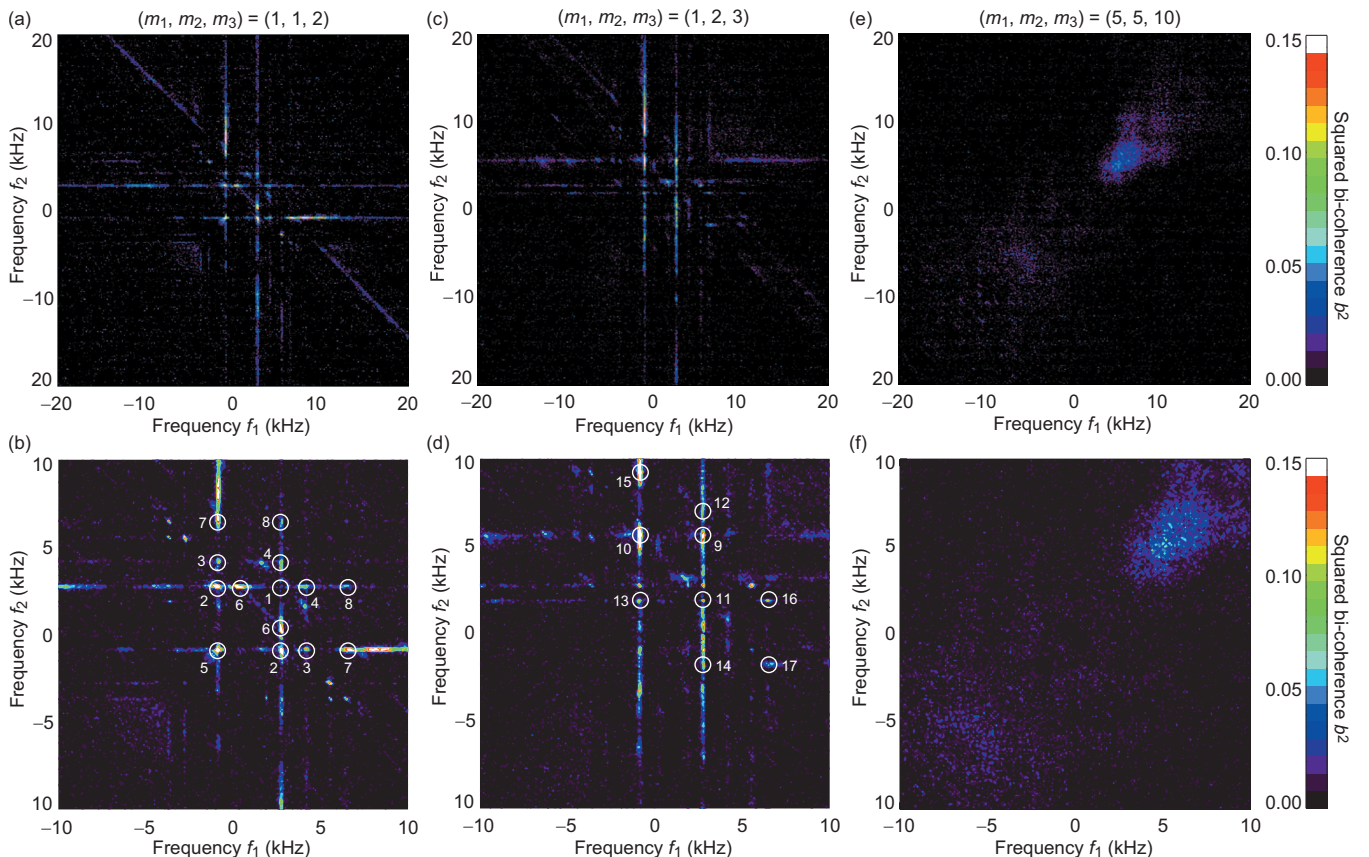


FIG. 6. (Color) Contour plots of squared bicoherence,  $b^2$ , between three waves  $(m_1, f_1)$ ,  $(m_2, f_2)$ , and  $(m_3, f_3)$ , which satisfy the matching conditions  $(m_1, m_2, m_3) = [(a) \text{ and } (b)] (1, 1, 2)$ ,  $[(c) \text{ and } (d)] (1, 2, 3)$ , and  $[(e) \text{ and } (f)] (5, 5, 10)$ . Frequency ranges are  $[(a), (c), \text{ and } (e)] (-20 \text{ kHz} \leq f_{1,2} \leq 20 \text{ kHz}, -40 \text{ kHz} \leq f_3 \leq 40 \text{ kHz})$  and  $[(b), (d), \text{ and } (f)] (-10 \text{ kHz} \leq f_{1,2} \leq 10 \text{ kHz}, -20 \text{ kHz} \leq f_3 \leq 20 \text{ kHz})$ . Circles with numbers indicate the mode couplings.

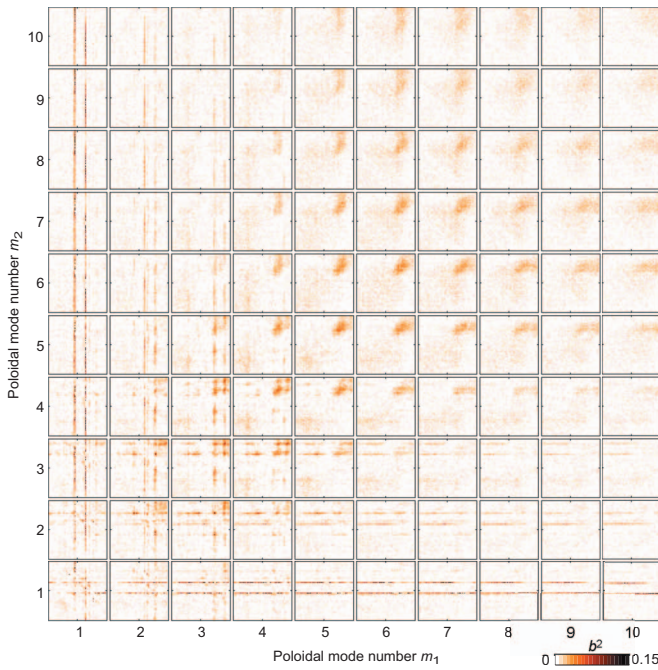


FIG. 7. (Color) Matrix of contour plots showing squared bicoherence,  $b^2$ . Each contour plot has frequency range of  $-10 \leq f_{1,2} \leq 10$  and  $-20 \leq f_3 \leq 20$ .

herence,  $b^2$ , to clarify the mode couplings among the waves with  $m=1, 2$ , and 3, or  $(m_1, m_2, m_3)=(1, 2, 3)$ . The confirmed nonlinear couplings are (9:G=A+D), (10:H=C+D), (11:H=A+E), (12:J=A+I), (13:O=C+E), (14:O=A+K), (15:G=C+N), (16:G=M+E), and (17:H=M+K). Thus, these nonlinear couplings were confirmed according to expectations.

In addition, Figs. 6(a)–6(d) clearly demonstrate the coupling between the modes and broadband components. For instance, the vertical line evident at  $f_1=2.8$  kHz in Fig. 6(c) indicates the presence of coupling between mode (A), broadband fluctuation components ( $m_2=2$ , in the frequency range of  $-8$  kHz  $< f_2 < 10$  kHz), and other broadband components ( $m_3=3$ ,  $-5.2$  kHz  $< f_3 < 12.8$  kHz). This indicates the presence of energy transfer between the mode and broadband fluctuations. Figures 6(e) and 6(f), which are the squared bicoherence,  $b^2$ , with  $(m_1, m_2, m_3)=(5, 5, 10)$ , show the coupling among the broadband components. This indicates the presence of energy exchange among broadband fluctuations.

Figure 7 is a matrix whose elements correspond to the bicoherence map between frequencies with a fixed combination of mode numbers. The columns and rows indicate the mode numbers ( $m_1$  and  $m_2$ ) from  $m=1$  to  $m=10$  and the map that occupies each position satisfies the matching condition,  $m_1+m_2=m_3$ . In each bicoherence map, the horizontal and vertical axes are  $f_1$  and  $f_2$ , respectively, with frequency ranges  $-10$  kHz  $\leq f_{1,2} \leq 10$  kHz and  $-20$  kHz  $\leq f_3 \leq 20$  kHz. The element at the left-bottom corner of the matrix is the same as Fig. 6(b), while the element directly above that is the same as Fig. 6(d). There are several features observable in Fig. 7. For low poloidal mode numbers ( $1 \leq m \leq 3$ ), the nonlinear couplings among fluctuation modes are clearly discernible. On the other hand, for high poloidal mode numbers ( $m \geq 4$ ), the nonlinear couplings among

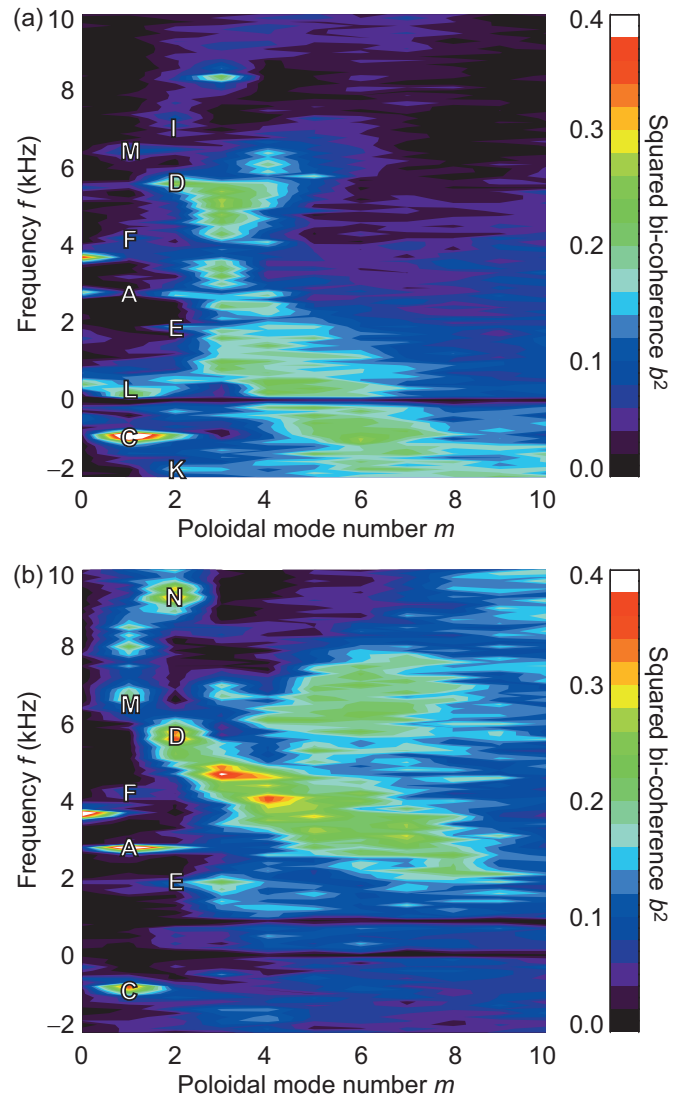


FIG. 8. (Color) Contour plot of squared bicoherence,  $b^2$ , between three waves; (a) [(a),  $(m, f)$ ,  $(m+1, f+2.8$  kHz)] and (b) [(c),  $(m, f)$ ,  $(m+1, f-0.9$  kHz)].

broadband fluctuations are the most obvious feature, showing that the energy exchange among broadband components is dominant in a wide high- $m$  region.

As for the left-side column (or the bottom row, i.e.,  $m=1$ ), the strongest couplings occur with modes (A) and (C), as shown in Figs. 6(a)–6(d). The modes are strongly coupled not only with the peaks but also with the broadband fluctuation components. To examine the couplings with the modes (A) and (C) in detail, Fig. 8 shows another expression of the bicoherence. In Fig. 8(a), the poloidal mode number,  $m_1$ , and frequency,  $f_1$ , are fixed to those of mode (A), that is,  $(m_1, f_1)=(1, 2.8$  kHz). The horizontal axis,  $m$ , and vertical axis,  $f$ , correspond to  $m_2$  and  $f_2$ , respectively. The contour shows the squared bicoherence of each wave  $(m, f)$  with (A) [( $m_3, f_3$ )= $(m+1, f+2.8$  kHz)]. Figure 8(a) indicates that the strongest nonlinear coupling is with mode (C), (2:E=A+C). Similarly, Fig. 8(b) where  $(m_1, f_1)=(1, -0.9$  kHz) shows the couplings with mode (C). The strongest nonlinear couplings are (2:E=A+C) and (5:K=C+C).

The separation of components with different poloidal

mode numbers has allowed us to identify several paths of nonlinear interaction among broadband components. First, the principal mode (A) nonlinearly couples with the  $m_2=1$  broadband component ( $f_2$ ). This process dominantly occurs when  $f_2 < 0$  (in the direction of ion diamagnetic drift). Second, when  $m_1=1$  but  $m_2$  is larger than 1, the frequency range of the broadband components covers all values in this frequency domain. Third, when both  $m_1$  and  $m_2$  are greater than 3, the coupling between three broadband components becomes dominant. Once some portion of the broadband fluctuations emerges, the coupling between this component and a low-index mode ( $m=1$  or 2 or 3) induces another broadband component at different mode numbers. Coupling between one broadband component ( $m_1$ ) and another ( $m_2$ ) induces a third ( $m_1+m_2$ ). Thus, turbulent energy can be distributed widely among broadband components.

It is important to compare the observed value of  $b^2(p, \omega)$  with theoretical predictions. The theoretical estimate of bicoherence is given in Ref. 38, and details of the method of comparison are discussed in Appendix B. The interaction between the modes (A, C, and E), which is observed as a peak in the squared bicoherence in Fig. 8(b) is compared with the theoretical estimate of 0.45. The experimentally determined peak value is about 0.54 as shown in Fig. 8(b), which is close to theoretically expected value. While noting the fact that the theoretical value is a crude estimate, employing the assumption that the  $E \times B$  nonlinearity in vorticity equation is dominant nonlinear mechanism, it is encouraging that it is the same order of magnitude as the experimental observation. This similarity leads to two conclusions. First, it suggests that the convective nonlinearity of the  $E \times B$  motion in the vorticity equation (which is kept in, e.g., Ref. 38) plays a dominant role in the nonlinear interactions of the plasma turbulence observed in the LMD-U device. Second, it provides a support for the analysis in Ref. 39, which evaluated the energy transfer from drift waves to zonal flows by assuming that the nonlinear interaction is given by the  $E \times B$  nonlinearity. This result is the same as the case of drift wave interaction in the edge turbulence of tokamaks.<sup>40</sup> Noting that the poloidal mode numbers could not be discriminated in Ref. 40, we stress that our use of bicoherence analysis on poloidally decomposed fluctuations provides a more quantitative conclusion for the nature of the nonlinear interaction of drift wave fluctuations.

## V. DIRECTION OF ENERGY TRANSFER

Bicoherence analysis can only confirm the existence of mode coupling between three waves, but cannot determine the causal relationship between the modes or which mode is the quasimode generated by the other two modes. Modes (A) and (C) are stronger and more stationary in time than the other modes, which appear intermittently with short lifetimes. Moreover, modes (A) and (C) have long correlation lengths and are produced globally in the poloidal direction.<sup>35</sup> Therefore, it is natural to conclude that modes (A) and (C) are the original parent modes. On the other hand, both modes (B) and (F) may be the third parent mode, although the linear

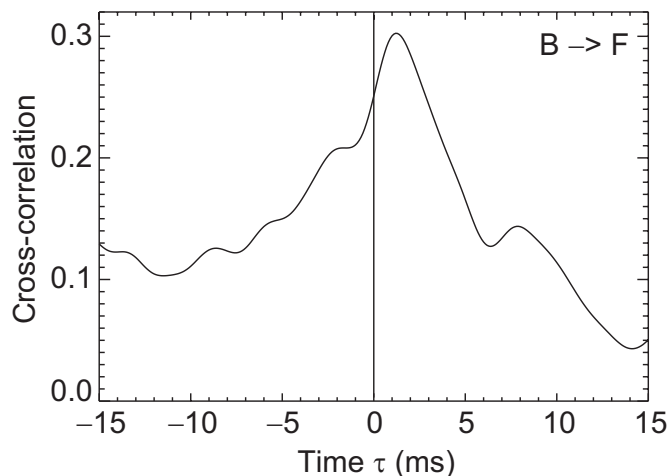


FIG. 9. Cross-correlation function,  $C_{BF}(\tau)$ , between time evolutions of wave amplitudes.  $\tau$  of the peak indicates time delay of mode (f) from mode (b). Data is an ensemble-average of eight discharges and indicates that mode (f) varies after mode (b) does.

dispersion relation calculated by numerical simulation suggests that the original parent mode is mode (B).

In order to verify the hypothesis that mode (B) is the original parent mode, the energy transfer direction must be evaluated. Several methods have been proposed to determine the energy transfer direction, such as bispectral analysis assuming a Hasegawa–Mima type three-wave coupling equation.<sup>9,25,29,30</sup> Here we choose the ACT<sup>19,20,31</sup> to estimate the energy transfer direction. This method simply deduces the causality or energy transfer direction from the temporal relation between the modes, based on the fact that the parent mode should vary earlier than the child mode in time. Bispectral analysis can directly estimate the coupling coefficient and energy transfer direction between three waves if a simple quadratic nonlinearity is assumed. However, in our analysis using ACT, the poloidal mode-decomposition with the 64-channel probe array provides very noiseless data, which makes it possible to better evaluate the causality between the modes of concern.

ACT was applied to investigate the time delay between the power spectrum variations of modes (B) and (F) (see Appendix C for the calculation method), although ACT does not determine the mechanism of energy transfer. Figure 9 shows the cross-correlation function,  $C_{BF}(\tau)$ , between the time evolutions of the amplitudes of modes (B) and (F) ( $\sigma$  of the window function is 1 ms, and  $\tau$  in Eq. (C2) of Appendix C moves every 0.1 ms). According to Appendix C, the position  $\tau$  of the peak of  $C_{BF}(\tau)$  indicates the response time of mode (F) to the variation of mode (B). The peak of  $C_{BF}(\tau)$  is seen at  $\tau=1.2$  ms, which indicates that mode (F) responds 1.2 ms after a variation of mode (B). Even when different values of  $\sigma$  were provided, it was found that mode (F) responds 1–2 ms after mode (B) varies. From this fact, mode (B) is deduced to be the parent mode. To express the energy transfer direction precisely, the nonlinear coupling process can be rewritten as  $(B-C \Rightarrow F)$  or  $(B+C^* \Rightarrow F)$ .

Based on the above analysis, the three original parent modes are (A, B, and C). All the other waves (D–O) are

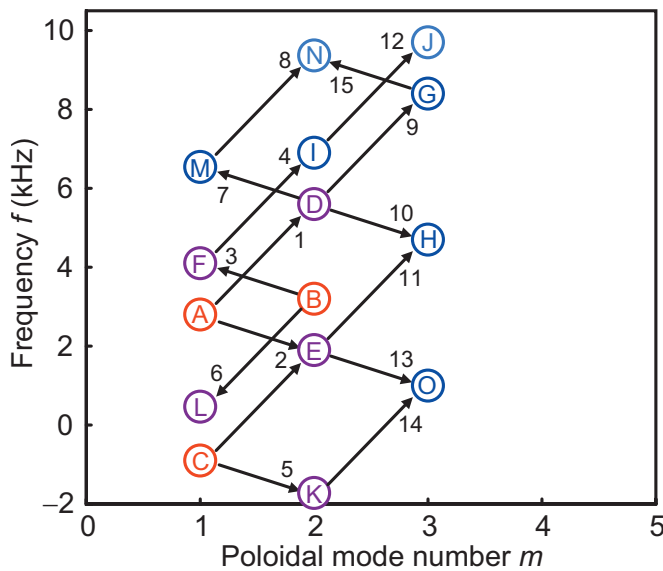


FIG. 10. (Color) Schematic showing successive generation of quasimodes from the three original parent modes (A, B, and C). Arrows point from parent mode to child mode. Numbers near the arrows are consistent with the numbers used in Fig. 6. Only the arrows 1, 2, and 5 are shown from modes [(a) and (c)].

quasimodes, which are successively generated by nonlinear mode couplings from modes (A), (B), and (C). Figure 10 is a summarized chart of the provided results. The schematic shows the successive generation of the quasimodes from the original parent modes. The numbers in the figure are the same as those used in Fig. 6. The arrows with numbers (16: M, E  $\rightarrow$  G) and (17: M, K  $\rightarrow$  H) are omitted from the figure to avoid confusion. The arrows go from the parent modes to the child modes. Modes (D, E, F, K, and L) are the quasimodes of the first generation, modes (G, H, I, M, and O) are those of the second generation, and modes (J, N) are those of the third generation. It can be seen that there are more than three paths to create (H) from the parent modes (A) and (C); one from (D), another from (E), and yet another from (M) and (K). By the same argument, (G), (N), and (O) are also produced from multiple coupling paths. Considering this fact, the direction of the arrows becomes ambiguous as the quasimodes become further and further generationally removed from the parent modes. The results reveal that cascading processes toward high- $m$  and high- $f$  develop via nonlinear couplings and add to the drift wave turbulence. In other words, a few number of parent modes excite successive quasimodes and broadband fluctuations, which do not satisfy the linear dispersion relation of the drift wave in  $m$ - $f$  space.

## VI. SUMMARY

The 2D (poloidal mode number  $m$  and frequency  $f$ ) power spectrum of the fluctuations in the normalized ion saturation-current was measured using a 64-channel poloidal Langmuir probe array in LMD-U. 2D bispectral analysis, which considers both the matching conditions of  $m$  and  $f$  was applied to the ion saturation-current fluctuation and confirmed the existence of nonlinear coupling between the peaks and broadband fluctuations. Nonlinear coupling between the

broadband fluctuations were confirmed in the high- $m$  and high- $f$  region. A number of pronounced peaks were revealed to have three irreducible original parent modes. Employing the drift wave linear dispersion relation calculated with a numerical simulation and the ACT, which roughly estimates the energy transfer direction, the three original parent modes were found to be  $(m, f) = (1, 2.8 \text{ kHz})$ ,  $(2, 3.2 \text{ kHz})$ , and  $(1, -0.9 \text{ kHz})$ . Other peaks and broadband fluctuations were quasimodes, which were generated by nonlinear mode coupling of the three original parent modes. A comparison between a theoretical estimate and the experimentally observed bicoherence indicated that the convective nonlinearity of  $E \times B$  motion plays a dominant role in the nonlinear interactions of the plasma turbulence observed in the LMD-U device. This use of bicoherence analysis on poloidally decomposed fluctuations provides a more quantitative understanding of the nonlinear interaction of drift wave fluctuations in LMD-U.

## ACKNOWLEDGMENTS

This work was supported by a Grant-in-Aid for Scientific Research (S) of JSPS (Grant No. 21224014), a Grant-in-Aid for Young Scientists (B) of JSPS (Grant No. 21760688), the collaboration programs of NIFS (Contract No. NIFS10KOAP023) and RIAM, Kyushu University, and the Asada Eiichi Research Foundation.

## APPENDIX A: 2D SPECTRAL AND BISPECTRAL ANALYSES

In this section, we provide explanations of the 2D spectral and bispectral analyses applied to multichannel poloidal probe array measurements. When there are  $M$  probe tips along the poloidal direction ( $\theta$ ) with equal spacing, the poloidal mode number,  $m$ , of the fluctuation wave ( $m$  is an integer;  $|m| \leq M/2$ ) is measurable. Here, the poloidal angle,  $\theta$ , equals  $2\pi i/M$ , where  $i$  is an integer. When the time evolution is obtained for  $N$  points with time resolution  $\Delta t$ , the time is an integer multiple of the time resolution,  $t = j\Delta t$ . From the spatiotemporal discrete waveform data,  $z_{ij}$ , 2D Fourier-transformed discrete data,  $Z_{mk}$ , are calculated as

$$Z_{mk} = \frac{1}{MN} \sum_{i=0}^{M-1} \sum_{j=0}^{N-1} z_{ij} \exp \left[ 2\pi i I \left( \frac{im}{M} - \frac{jk}{N} \right) \right], \quad (\text{A1})$$

where  $I$  is the imaginary unit ( $I^2 = -1$ ) and  $k$  is an integer ( $|k| \leq N/2$ ). The frequency,  $f$ , takes values  $k\Delta f$ , where  $\Delta f = 1/(N\Delta t)$  is the frequency resolution. The power spectrum,  $S_{mk}$ , is calculated from  $Z_{mk}$  by  $S_{mk} = |Z_{mk}|^2 / \Delta f$ . The poloidal mode number,  $m$ , is related to the poloidal wave number,  $k_\theta$ , by  $m = r_p k_\theta$ , where  $r_p$  is the radius of the probe array. Thus, the 2D waveform,  $z(\theta, t)$ , is transformed to  $Z(m, f)$  by 2D Fourier transformation. Since  $Z(-m, -f) = Z^*(m, f)$ ,  $S(-m, -f) = S(m, f)$ . It means, the fluctuations  $(m, f)$  and  $(-m, -f)$  are physically identical. Therefore, we need to keep only  $m \geq 0$  (or  $f \geq 0$ ). In this paper,  $m \geq 0$  has been chosen, so that  $0 \leq m \leq M/2$  and  $-(2\Delta t)^{-1} < f \leq (2\Delta t)^{-1}$ .

Bispectral analysis<sup>28</sup> examines the relationship between three fluctuation waves that satisfy the matching conditions

for both the wave number and frequency. When the wave numbers and frequencies of the three waves are  $(\mathbf{k}_1, \omega_1)$ ,  $(\mathbf{k}_2, \omega_2)$ , and  $(\mathbf{k}_3, \omega_3)$ , respectively, the matching conditions are  $(\mathbf{k}_1 + \mathbf{k}_2 = \mathbf{k}_3)$  and  $(\omega_1 + \omega_2 = \omega_3)$ . With a poloidal probe array, the poloidal mode number,  $m = r_p k_\theta$ , of the fluctuation wave is measurable, as well as the frequency,  $f = \omega/2\pi$ . In this paper, we define 2D bispectral analysis as bispectral analysis which takes into consideration the matching conditions of the poloidal mode number,  $m_1 + m_2 = m_3$ , and frequency,  $f_1 + f_2 = f_3$ . When the 2D Fourier transformed expression,  $Z(m, f)$ , of the three waves are  $Z_1 = Z(m_1, f_1)$ ,  $Z_2 = Z(m_2, f_2)$ , and  $Z_3 = Z(m_3, f_3)$ , the bispectrum,  $B$ , of the three waves is expressed as  $B = \langle Z_1 Z_2 Z_3^* \rangle$ . When the three waves fluctuate independently, the absolute value,  $|B|$ , becomes 0. When the phases of the three waves are connected by a certain relationship,  $|B|$  becomes finite. The bicoherence,  $b$ , which is a normalized value of  $B$ , and the biphase,  $\phi_b$ , which shows the relationship among the phases of the three waves, are expressed as

$$b^2 = \frac{|B|^2}{\langle |Z_1 Z_2|^2 \rangle \langle |Z_3|^2 \rangle}, \quad (\text{A2})$$

$$\phi_b = \tan^{-1} \frac{\text{Im}(B)}{\text{Re}(B)}, \quad (\text{A3})$$

respectively. Bicoherence analysis is important for investigating the coupling between three waves. When the bicoherence,  $b$ , is finite for three waves, it suggests that one wave is produced by nonlinear mode coupling of the other two waves.

## APPENDIX B: COMPARISON WITH THEORETICAL ESTIMATE

The comparison of the bispectrum with the theoretical prediction of Ref. 38 was not trivial. The case was studied where the nonlinear dynamical equation is written in a form

$$\frac{\partial}{\partial t} g + (-\gamma + iL_0)g = \sum N g g, \quad (\text{B1})$$

where  $g$  stands for a dynamical variable of interest (such as the normalized density perturbation),  $\gamma$  is a linear growth rate,  $L_0$  represents the linear frequency, and  $N$  denotes the coefficient of the nonlinear interaction. (In general,  $N$  may include operators.) Fourier components are introduced as  $g(t) = \sum_p g_p \exp(-ipt)$ .

In order to calculate the bispectrum for the component  $g_\omega$ , the nonlinear term  $N_{p,\omega} g_p g_{p-\omega} g_\omega$  is extracted from the total of all nonlinear terms,  $\sum N g g$ .<sup>41,42</sup> The nonlinear response of the component  $g_p$  against the imposition of a test mode  $g_\omega$  is expressed as  $g_p \approx \tau_p N_{p,\omega} g_p g_{p-\omega} g_\omega + \tilde{g}_p$ , where  $\tau_p$  is the nonlinear interaction time, and  $\tilde{g}_p$  represents the excitation through interaction with other modes and is statistically independent from  $g_{p-\omega} g_\omega$ . The bicoherence indicator is expressed in terms of the second-order correlation functions and the nonlinear coupling coefficient,  $N$ , as<sup>38</sup>

$$B(p, \omega) = \tau_p N_{p,\omega}^* \langle |g_{p-\omega}|^2 |g_\omega|^2 \rangle + \tau_{p-\omega} N_{p-\omega,p} \langle |g_p|^2 |g_\omega|^2 \rangle + \tau_\omega N_{\omega,p} \langle |g_{p-\omega}|^2 |g_p|^2 \rangle. \quad (\text{B2})$$

We consider the case of interaction among sharp peaks, e.g., the combination of (A, C, and E). We take  $\omega$ ,  $p$ , and  $p-\omega$ , for modes (E), (A), and (C), respectively, and find that the third term in Eq. (B2) dominates over the first and second terms because mode (E) has the smallest amplitude of (A, C, and E). The squared bicoherence is evaluated by following Ref. 38 as

$$b^2(p, \omega) \approx |\tau_\omega N_{E,A}|^2 \frac{\langle |g_C|^2 \rangle}{\langle |g_E|^2 \rangle} \langle |g_p|^2 \rangle, \quad (\text{B3})$$

where  $\tau_\omega$  is the autocorrelation time of mode (E),  $N_{E,A}$  is the nonlinear interaction between modes (E) and (A),  $\langle |g_C|^2 \rangle / \langle |g_E|^2 \rangle$  is the ratio of fluctuation intensities of modes (C) and (E), and  $\langle |g_p|^2 \rangle$  is the power spectrum near the peak of mode (A). Note that the frequency variable  $p$  corresponds to the vertical axis  $f$  in Fig. 8(b) and we are considering the peak “(A)” in Fig. 8(b).

The interaction of drift waves through the convective nonlinearity of the  $E \times B$  motion, i.e.,  $V_{E \times B} \nabla V_{E \times B}$  term, has been studied in Ref. 38. The coupling coefficient of this mechanism was evaluated as  $|N| \sim (c_s/2\rho_s) k_\perp^4 \rho_s^4 (1 + k_\perp^2 \rho_s^2)^{-1}$  for drift wave fluctuations. If the nonlinear coupling between (A), (C), and (E) is dominated by the Lagrange nonlinearity of the  $E \times B$  motion, then the squared bicoherence is given by

$$b^2(p, \omega) \sim \left| \frac{\tau_\omega c_s}{2\rho_s} \frac{k_\perp^4 \rho_s^4}{1 + k_\perp^2 \rho_s^2} \right|^2 \frac{\langle |g_C|^2 \rangle}{\langle |g_E|^2 \rangle} \langle |g_p|^2 \rangle. \quad (\text{B4})$$

We compare the theoretical prediction of Eq. (B4) with the observed value of  $b^2(p, \omega)$ . This comparison provides a test for whether the nonlinearity of interest is dominant in the observed turbulence. The experimentally observed value of  $b^2(p, \omega)$  is compared with this theoretical estimate. Parameters are acquired from the experiment as follows:  $\tau_\omega$  is given by the full width at half maximum of the spectrum peak of mode (E) as  $\tau_\omega \sim 4 \times 10^{-3}$  s,  $c_s/\rho_s \sim 4.4 \times 10^4$  Hz,  $k_\perp \sim 35$  m<sup>-1</sup>,  $k_\perp \rho_s \sim 0.4$ , and  $\langle |g_C|^2 \rangle / \langle |g_E|^2 \rangle \sim 12$ . Substituting these numbers into Eq. (B4) provides a theoretical estimate of  $b^2(p, \omega) \sim 45 \langle |g_p|^2 \rangle$ . When measuring the bicoherence, the frequency window is taken to be 100 Hz, i.e., the discrete power spectrum  $\langle |g_p|^2 \rangle$  is given by integrating  $S(m, f)$  over a window of width 100 Hz. That is, the peak of the normalized fluctuation of the ion saturation-current of mode (A) is  $\langle |g_p|^2 \rangle \approx 0.01$  in the experiment. Substituting these numbers, the squared bicoherence for the coupling between modes (A), (C), and (E) is theoretically estimated to have a peak value of 0.45. The experimentally observed peak value is about 0.54, as shown in Fig. 8(b). The observation is close to the theoretical expectation.

While noting the fact that the theoretical estimate, Eq. (B4), is quite crude using the assumption that the  $E \times B$  nonlinearity is the dominant nonlinear mechanism, it nevertheless gives a result that is the same order of magnitude as the experimental observation. This similarity leads to two conclusions. First, it suggests that the  $E \times B$  nonlinearity plays a

dominant role in the nonlinear interactions of the plasma turbulence observed in the LMD-U device. (More rigorously put, the working hypothesis that the  $E \times B$  nonlinearity has a dominant role is not rejected by this comparison.) Second, this comparison lends support to the analysis in Ref. 39, where the energy transfer to the zonal flow from drift waves was evaluated by assuming that the nonlinear interaction fully described by the  $E \times B$  nonlinearity.

This result is the same as the case of drift wave interactions in the edge turbulence of tokamaks.<sup>40</sup> Noting the fact that the poloidal mode numbers could not be discriminated in Ref. 40, we stress that our use of bicoherence analysis on poloidally decomposed fluctuations provides more a quantitative conclusion for the nature of the nonlinear interaction of plasma turbulence.

### APPENDIX C: AMPLITUDE CORRELATION TECHNIQUE

The ACT is carried out by comparing the time evolutions of the powers of two waves.  $S_X(t) = S(m_X, f_X, t)$  is the time evolution of the amplitude of a certain wave (X), calculated by the Gabor transformation. The Gabor transformation is a short-time Fourier transformation which uses a Gaussian type of window function,  $w(t) = \exp(-t^2/\sigma^2)$ . When the spatiotemporal waveform,  $z(\theta, t)$ , is mode-decomposed to  $Z(m, t)$  by 1D Fourier transformation, the time evolution of the wave amplitude,  $S(m, f, t)$ , is calculated by

$$S(m, f, t) = \left| \int Z(m, t') w(t' - t) e^{-2\pi i f t'} dt' \right|^2. \quad (\text{C1})$$

The parameter  $\sigma$  of the window function determines the time width used to calculate  $S(m, f, t)$ . When  $\sigma$  is large, the time width is large and the frequency resolution is sharp.

The cross-correlation function between  $S_X(t)$  and  $S_Y(t)$  is evaluated as

$$C_{XY}(\tau) = \frac{\langle [S_X(t) - \bar{S}_X][S_Y(t + \tau) - \bar{S}_Y] \rangle}{\sqrt{\langle [S_X(t) - \bar{S}_X]^2 \rangle \langle [S_Y(t) - \bar{S}_Y]^2 \rangle}}, \quad (\text{C2})$$

where  $\bar{S}_{X,Y}$  are long time averages of  $S_{X,Y}(t)$ , respectively. When the amplitude of the two waves varies similarly in time, a peak in the cross-correlation function appears near  $\tau=0$ , and the position  $\tau$  of the peak indicates the time response of  $S_Y(t)$  to  $S_X(t)$ .

<sup>1</sup>P. H. Diamond, S.-I. Itoh, K. Itoh, and T. S. Hahm, *Plasma Phys. Controlled Fusion* **47**, R35 (2005).

<sup>2</sup>M. Kono and M. Y. Tanaka, *Phys. Rev. Lett.* **84**, 4369 (2000).

<sup>3</sup>C. Holland, G. R. Tynan, J. H. Yu, A. James, D. Nishijima, M. Shimada, and N. Taheri, *Plasma Phys. Controlled Fusion* **49**, A109 (2007).

<sup>4</sup>N. Kasuya, M. Yagi, K. Itoh, and S.-I. Itoh, *Phys. Plasmas* **15**, 052302 (2008).

<sup>5</sup>V. Sokolov and A. K. Sen, *Phys. Rev. Lett.* **92**, 165002 (2004).

<sup>6</sup>V. Sokolov, X. Wei, A. K. Sen, and K. Avinash, *Plasma Phys. Controlled Fusion* **48**, S111 (2006).

<sup>7</sup>G. R. Tynan, C. Holland, J. H. Yu, A. James, D. Nishijima, M. Shimada, and N. Taheri, *Plasma Phys. Controlled Fusion* **48**, S51 (2006).

<sup>8</sup>C. Holland, J. H. Yu, A. James, D. Nishijima, M. Shimada, N. Taheri, and G. R. Tynan, *Phys. Rev. Lett.* **96**, 195002 (2006).

<sup>9</sup>M. Xu, G. R. Tynan, C. Holland, Z. Yan, S. H. Muller, and J. H. Yu, *Phys. Plasmas* **16**, 042312 (2009).

<sup>10</sup>C. M. Ryu and T. Rhee, *Fusion Sci. Technol.* **51**, 92 (2007).

<sup>11</sup>A. Okamoto, K. Hara, K. Nagaoka, S. Yoshimura, J. Vranješ, M. Kono, and M. Y. Tanaka, *Phys. Plasmas* **10**, 2211 (2003).

<sup>12</sup>A. Latten, T. Klinger, A. Piel, and Th. Pierre, *Rev. Sci. Instrum.* **66**, 3254 (1995).

<sup>13</sup>T. Klinger, A. Latten, A. Piel, G. Bonhomme, T. Pierre, and T. Dudok de Wit, *Phys. Rev. Lett.* **79**, 3913 (1997).

<sup>14</sup>C. Schröder, T. Klinger, D. Block, A. Piel, G. Bonhomme, and V. Naulin, *Phys. Rev. Lett.* **86**, 5711 (2001).

<sup>15</sup>T. Kaneko, H. Tsunoyama, and R. Hatakeyama, *Phys. Rev. Lett.* **90**, 125001 (2003).

<sup>16</sup>C. Schröder, O. Grulke, and T. Klinger, *Phys. Plasmas* **12**, 042103 (2005).

<sup>17</sup>F. Brochard, T. Windisch, O. Grulke, and T. Klinger, *Phys. Plasmas* **13**, 122305 (2006).

<sup>18</sup>A. Fujisawa, K. Itoh, H. Iguchi, K. Matsuoka, S. Okamura, A. Shimizu, T. Minami, Y. Yoshimura, K. Nagaoka, C. Takahashi, M. Kojima, H. Nakano, S. Ohsima, S. Nishimura, M. Isobe, C. Suzuki, T. Akiyama, K. Ida, K. Toi, S.-I. Itoh, and P. H. Diamond, *Phys. Rev. Lett.* **93**, 165002 (2004).

<sup>19</sup>H. Xia and M. G. Shats, *Phys. Rev. Lett.* **91**, 155001 (2003).

<sup>20</sup>M. G. Shats, H. Xia, and H. Punzmann, *Phys. Rev. E* **71**, 046409 (2005).

<sup>21</sup>Y. Nagashima, K. Hoshino, A. Ejiri, K. Shinohara, Y. Takase, K. Tsuzuki, K. Uehara, H. Kawashima, H. Ogawa, T. Ido, Y. Kusama, and Y. Miura, *Phys. Rev. Lett.* **95**, 095002 (2005).

<sup>22</sup>C. Hidalgo, M. A. Pedrosa, E. Sánchez, B. Gonçalves, J. A. Alonso, E. Calderón, A. A. Chmyga, N. B. Dreval, L. Eliseev, T. Estrada, L. Krupnik, A. V. Melnikov, R. O. Orozco, J. L. de Pablos, and C. Silva, *Plasma Phys. Controlled Fusion* **48**, S169 (2006).

<sup>23</sup>N. Krause, C. Lechte, J. Stöber, U. Stroth, E. Ascasibar, J. Alonso, and S. Niedner, *Rev. Sci. Instrum.* **73**, 3474 (2002).

<sup>24</sup>U. Stroth, F. Greiner, C. Lechte, N. Mahdizadeh, K. Rahbarnia, and M. Ramisch, *Phys. Plasmas* **11**, 2558 (2004).

<sup>25</sup>P. Manz, M. Ramisch, U. Stroth, V. Naulin, and B. D. Scott, *Plasma Phys. Controlled Fusion* **50**, 035008 (2008).

<sup>26</sup>P. Manz, M. Ramisch, and U. Stroth, *Plasma Phys. Controlled Fusion* **51**, 035008 (2009).

<sup>27</sup>F. M. Poli, P. Ricci, A. Fasoli, and M. Podestà, *Phys. Plasmas* **15**, 032104 (2008).

<sup>28</sup>Y. C. Kim and E. J. Powers, *Phys. Fluids* **21**, 1452 (1978).

<sup>29</sup>Ch. P. Ritz, E. J. Powers, and R. D. Bengtson, *Phys. Fluids B* **1**, 153 (1989).

<sup>30</sup>J. S. Kim, R. D. Durst, R. J. Fonck, E. Fernandez, A. Ware, and P. W. Terry, *Phys. Plasmas* **3**, 3998 (1996).

<sup>31</sup>F. J. Crossley, P. Uddholm, P. Duncan, M. Khalid, and M. G. Rusbridge, *Plasma Phys. Controlled Fusion* **34**, 235 (1992).

<sup>32</sup>K. Terasaka, S. Shinohara, Y. Nagashima, T. Yamada, M. Kawaguchi, T. Maruta, S. Inagaki, Y. Kawai, N. Kasuya, M. Yagi, A. Fujisawa, K. Itoh, and S.-I. Itoh, *Plasma Fusion Res.* **2**, 031 (2007).

<sup>33</sup>T. Yamada, Y. Nagashima, S. Inagaki, Y. Kawai, M. Yagi, S.-I. Itoh, T. Maruta, S. Shinohara, K. Terasaka, M. Kawaguchi, M. Fukao, A. Fujisawa, and K. Itoh, *Rev. Sci. Instrum.* **78**, 123501 (2007).

<sup>34</sup>T. Yamada, S.-I. Itoh, T. Maruta, S. Shinohara, N. Kasuya, Y. Nagashima, M. Yagi, K. Terasaka, M. Kawaguchi, S. Inagaki, Y. Kawai, M. Fukao, A. Fujisawa, and K. Itoh, *Plasma Fusion Res.* **2**, 051 (2007).

<sup>35</sup>T. Yamada, S.-I. Itoh, K. Terasaka, N. Kasuya, Y. Nagashima, S. Shinohara, T. Maruta, M. Yagi, S. Inagaki, Y. Kawai, A. Fujisawa, and K. Itoh, *Plasma Fusion Res.* **3**, 044 (2008).

<sup>36</sup>T. Yamada, S.-I. Itoh, T. Maruta, N. Kasuya, Y. Nagashima, S. Shinohara, K. Terasaka, M. Yagi, S. Inagaki, Y. Kawai, A. Fujisawa, and K. Itoh, *Nat. Phys.* **4**, 721 (2008).

<sup>37</sup>B. B. Kadomtsev, *Plasma Turbulence* (Academic, London, 1965), p. 53.

<sup>38</sup>K. Itoh, Y. Nagashima, S.-I. Itoh, P. H. Diamond, A. Fujisawa, M. Yagi, and A. Fukuyama, *Phys. Plasmas* **12**, 102301 (2005).

<sup>39</sup>Y. Nagashima, S.-I. Itoh, S. Shinohara, M. Fukao, A. Fujisawa, K. Terasaka, Y. Kawai, G. R. Tynan, P. H. Diamond, M. Yagi, S. Inagaki, T. Yamada, and K. Itoh, *Phys. Plasmas* **16**, 020706 (2009).

<sup>40</sup>Y. Nagashima, K. Itoh, S.-I. Itoh, M. Yagi, A. Fujisawa, K. Hoshino, K. Shinohara, K. Uehara, Y. Kusama, A. Ejiri, and Y. Takase, *Rev. Sci. Instrum.* **77**, 045110 (2006).

<sup>41</sup>S.-I. Itoh and K. Itoh, *J. Phys. Soc. Jpn.* **68**, 1891 (1999).

<sup>42</sup>S.-I. Itoh and K. Itoh, *J. Phys. Soc. Jpn.* **69**, 427 (2000).